

# Giant optical second-harmonic generation in single and coupled microcavities formed from one-dimensional photonic crystals

Tatyana V. Dolgova, Anton I. Maidykovski, Michail G. Martemyanov, Andrey A. Fedyanin, and Oleg A. Aktsipetrov

*Department of Physics, Moscow State University, 119992 Moscow, Russia*

**Gerd Marowsky**

*Laser-Laboratorium Goettingen, Hans-Adolf-Krebs-Weg 1, D-37077 Goettingen, Germany*

**Vladimir A. Yakovlev**

*Institute of Spectroscopy, Russian Academy of Sciences, 142092 Troitsk, Russia*

**Giorgio Mattei**

*Istituto di Metodologie Avanzate Inorganiche, CNR, Area della Ricerca di Roma, C.P. 10, Monterotondo Scalo, 00016, Italy*

**Narumi Ohta and Seiichiro Nakabayashi**

*Department of Chemistry, Faculty of Science, Saitama University, Urawa, Japan*

Received December 11, 2001; revised manuscript received March 29, 2002; accepted April 16, 2002

The nonlinear optical properties of one-dimensional all-solid-state photonic-crystal microcavities (MCs) are experimentally studied by second-harmonic generation (SHG) spectroscopy in both the frequency and the wave-vector domains. The studied single and coupled MCs are formed by the alternating of mesoporous silicon layers of different porosities. When the fundamental radiation is in resonance with the MC mode the second-harmonic intensity is enhanced by a factor of approximately  $10^2$ . The resonant SHG response is compared with the off-resonance response, as the fundamental wavelength is outside the photonic bandgap. The splitting of the modes of two identical coupled MCs is observed in the wave-vector domain spectrum of enhanced SHG. The SHG enhancement is attributed to the combined effects of the spatial localization of the fundamental field in the MC spacer and the fulfillment of the phase-matching conditions. The confinement of the resonant fundamental field is probed directly at the MC cleavage by a scanning near-field optical microscope. The role of the phase matching that is associated with the giant effective dispersion in the spectral vicinity of the MC mode is deduced from a comparison with the SHG peaks at both edges of the photonic bandgap.

© 2002 Optical Society of America

OCIS codes: 190.2620, 230.4170.

## 1. INTRODUCTION

The considerable interest in photonic crystals from both the fundamental and the applied viewpoints is due to the potential use of the photonic bandgap (PBG) in controlling the emission and the propagation of light. The variety of spectacular properties of photonic crystals, such as suppression of group velocity,<sup>1,2</sup> inhibition of spontaneous emission,<sup>3</sup> and large birefringence,<sup>4,5</sup> can lead to many useful applications in integrated optics. Other effects are related to nonlinear optical properties of photonic crystals. For example, ultrafast optical switching<sup>6</sup> and bistability<sup>7</sup> can be observed in photonic crystals with cubic nonlinearity as a result of self-induced transparency, leading to a dynamic or a steady-state shift of the spectral position of the PBG. Other phenomena are enhanced frequency conversions, such as second-harmonic generation

(SHG) and sum-frequency generation. Enhancement of SHG can be achieved in nonlinear photonic crystals<sup>8,9</sup> by the reversal of the sign of the nonlinear polarization with a period equal to two coherence lengths to compensate for the phase mismatch between the fundamental and the second-harmonic (SH) waves. In the one-dimensional (1-D) case such quasi-phase matching was performed in GaAs waveguides<sup>10</sup> or in periodically poled lithium niobate.<sup>11</sup> Quasi-phase matching in two-dimensional nonlinear photonic crystals based on hexagonally poled lithium niobate was recently observed.<sup>12</sup> Phase matching in photonic crystals with periodic modulation of the refractive index can be achieved when the fundamental wavelength is tuned near the PBG edge.<sup>13</sup> SHG enhancement was observed in 1-D photonic crystals—distributed Bragg reflectors (DBRs), formed by GaAs/

AlGaAs,<sup>14</sup> AlAs/AlGaAs,<sup>15</sup> and ZnS/SrF<sub>2</sub> (Ref. 16) layers, or alternating layers of porous silicon (PS) with different porosities.<sup>17,18</sup>

Several approaches are used for the calculation of SHG enhancement at the PBG edges of photonic crystals. One operates with a dispersion relation for optical waves in 1-D periodic structures,<sup>19</sup> and the group velocity of the fundamental wave tends to zero at the PBG edges.<sup>20</sup> In this case the SH field generated is calculated by use of the slowly varying envelope approximation in time<sup>21</sup> or in the effective medium model.<sup>22</sup> Other approaches are based on the nonlinear transfer-matrix<sup>23</sup> or the Green's function<sup>24</sup> formalisms. The SHG gain at the PBG edges can also be calculated by use of the recurrence-relation method.<sup>25</sup>

One-dimensional photonic crystals with a modified or a replaced crystal cell act as microcavities (MCs) with distributed mirrors. The MC mode is located inside the photonic bandgap, and its spectral position with respect to the PBG center is defined by parameters of the MC spacer (thickness and refractive index). If the fundamental wave is in resonance with the MC mode, the fundamental field is strongly localized inside the MC, and the nonlinear optical response of the MC is enhanced. A few studies have been devoted to SHG enhancement in photonic-crystal MCs. A significant increase in the SH intensity generated from a monolayer of chromophores that were embedded in the air spacer between two dielectric DBRs was reported.<sup>26</sup> Resonant SHG in a poled-polymer layer squeezed between a silver mirror and a SiO<sub>2</sub>/TiO<sub>2</sub> DBR<sup>27</sup> and in a ZnSe MC with two SiO<sub>2</sub>/Si<sub>3</sub>N<sub>4</sub> DBRs<sup>28</sup> was recently demonstrated. The SHG resonances were achieved because of the confinement of the SH<sup>26,28</sup> or the fundamental<sup>27</sup> field in a MC spacer with a thickness smaller than the coherence length. Recently, the nonlinear magneto-optical Kerr effect in SHG was observed in 1-D magnetophotonic MCs built from two non-magnetic DBRs that were separated by a magnetic garnet half-wavelength-thick cavity spacer.<sup>29</sup> SHG spectroscopy of identical coupled MCs is a natural extension of the study of MCs with a single spacer. In these structures MC spacers are separated by an additional DBR. The electromagnetic coupling between cavities is controlled by variation of the separating DBR transmittance and leads to specific localization of the fundamental field. SHG enhancement in a 1-D coupled-resonator optical waveguide is predicted.<sup>30,31</sup>

A combination of phase matching and fundamental field confinement was used in a vertical MC with a spacer consisting of a quasi-phase-matched stack of alternating GaAs/AlAs layers.<sup>32</sup> However, the small *Q* factor of the MC restricted SHG enhancement. Another way to compensate for the destructive interference that is due to dispersive propagation in MCs with a dual-wavelength non-periodic DBR was proposed in Ref. 33. In photonic-crystal MCs consisting of a nonlinear spacer and nonlinear DBRs the SHG efficiency is significantly increased by the phase-mismatched compensation over the entire MC length and by the penetration of the resonant fundamental field into the DBR.

PS MCs are very attractive for all-silicon-based optoelectronic applications. The MCs consist of alternating

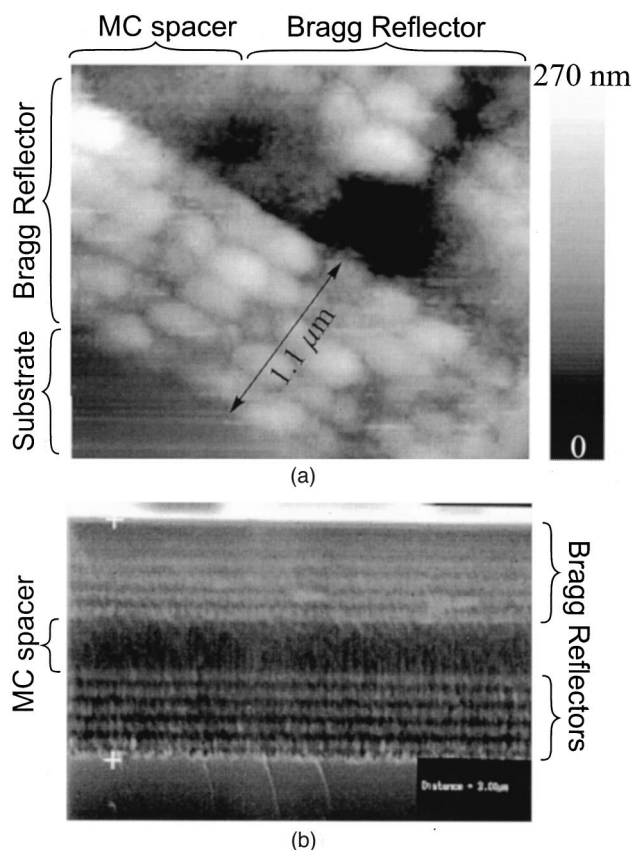


Fig. 1. (a) Scanning shear-force microscope image of the MC cleavage with  $\lambda_{MC} \approx 620$  nm. The scan area is  $1.8 \mu\text{m} \times 1.8 \mu\text{m}$ . (b) Scanning electron microscope image of the MC cleavage with  $\lambda_{MC} \approx 1700$  nm.

PS layers of differing porosities and, as a consequence, differing refractive indices. The spectral and the angular positions of the PBG and the MC mode can easily be tuned by one's controlling the thickness and the porosity of the PS layers.<sup>34</sup> The high quality of PS-based MCs is a result of optically flat layers with small interface corrugations and of the high contrast in refractive indices of adjacent layers. Various optical effects have been observed in PS photonic-crystal MCs (for a review, see Ref. 35). Recently, strong narrowing and enhancement of photoluminescence was demonstrated in single<sup>36</sup> and coupled<sup>37</sup> PS MCs. Raman scattering enhancement<sup>38</sup> and giant third-harmonic generation<sup>39</sup> were observed in PS MCs.

This paper focuses on experimental studies of resonant SHG in single and coupled MCs that are based on mesoporous-silicon photonic crystals. The contributions of resonant fundamental field localization and phase matching in the photonic-crystal MCs to SHG enhancement are derived from a comparison of experimental SHG spectra with numerical simulations within the nonlinear transfer-matrix formalism.<sup>23</sup> This approach is convenient for the analysis of partial SHG contributions of individual layers. Such an analysis manifests the features of the spatial distribution of optical fields and nonlinear sources in MCs. The paper is organized as follows: In Section 2 the details of single and coupled PS MC fabrication and experimental setups are presented. In Section 3 the experimental results of SHG spectroscopy in

the frequency and the wave-vector domains are shown. A scanning near-field optical microscope (SNOM) image of the MC is presented. In Section 4 a phenomenological description for SHG in 1-D photonic-crystal MCs is given. In Section 5 numerical results indicating the role of phase-matching and fundamental field confinement in SHG enhancement are discussed, and the experimental SHG results are compared to the numerical simulations. All results are summarized in Section 6. Detailed expressions for SHG in 1-D photonic-crystal MCs are derived in Appendix A.

## 2. SAMPLES AND SETUP

The PS photonic-crystal MCs are fabricated by use of techniques described in Ref. 35. Briefly, anodic etching in a HF(36%):C<sub>2</sub>H<sub>5</sub>OH solution (2:3 by volume) of the H-terminated Si (001) surface leads to the formation of the mesoporous-silicon layer. The H-terminated surface is obtained during a 5-min treatment of the natively oxidized *p*<sup>+</sup>-type Si (001) wafer with a resistivity of 0.01 Ω cm in the same etching solution. The PS layers with different porosities *f* (air fractional volume) and different thicknesses are obtained by the variation of the current density from 25 to 130 mA/cm<sup>2</sup> and an etching time of the order of several seconds. The dependences of the porosity and the etching rate on the current density are ex-

tracted from IR reflection spectra measured at single PS layers with a Fourier transform IR spectrometer. MCs with the MC mode centered at  $\lambda_{MC} \approx 945$  nm and  $\lambda_{MC} \approx 1300$  nm at normal incidence are composed of two DBRs separated by a MC spacer with an optical thickness of  $\lambda_{MC}/2$ . The bottom DBR is formed by 5 pairs of  $\lambda_{MC}/4$ -thick PS layers with high  $n_H$  and low  $n_L$  refractive indices, corresponding to porosities of  $f_H$  and  $f_L$ , respectively. The top DBR has 5.5 pairs for the sample with  $\lambda_{MC} \approx 945$  nm and 5 pairs for the sample with  $\lambda_{MC} \approx 1300$  nm. The cap low-refractive-index  $\lambda_{MC}/2$ -thick PS layer is grown on top of the first MC to lessen oxidation effects. The refractive indices of the first sample are  $n_H \approx 1.41$  and  $n_L \approx 1.18$  at 950 nm for porosities  $f_H \approx 0.77$  and  $f_L \approx 0.88$ , respectively. For the second sample the corresponding quantities are  $n_H \approx 2.0$ ,  $n_L \approx 1.65$ ,  $f_H \approx 0.6$ , and  $f_L \approx 0.7$  at 1064 nm. The MC spacer is fabricated from the low-refractive-index PS layer. For preparation of coupled-MC samples the time modulation of the current density is changed to obtain two identical  $\lambda_{MC}/2$ -thick spacers with  $\lambda_{MC} \approx 1250$  nm and separated and surrounded by DBRs. The intermediate DBR consists of 3.5 pairs of  $\lambda_{MC}/4$ -thick layers, and each external DBR consists of 4 pairs.

Independent characterization of the MC samples is performed by means of scanning shear-force and electron microscopy. Figure 1 shows images of two different MC

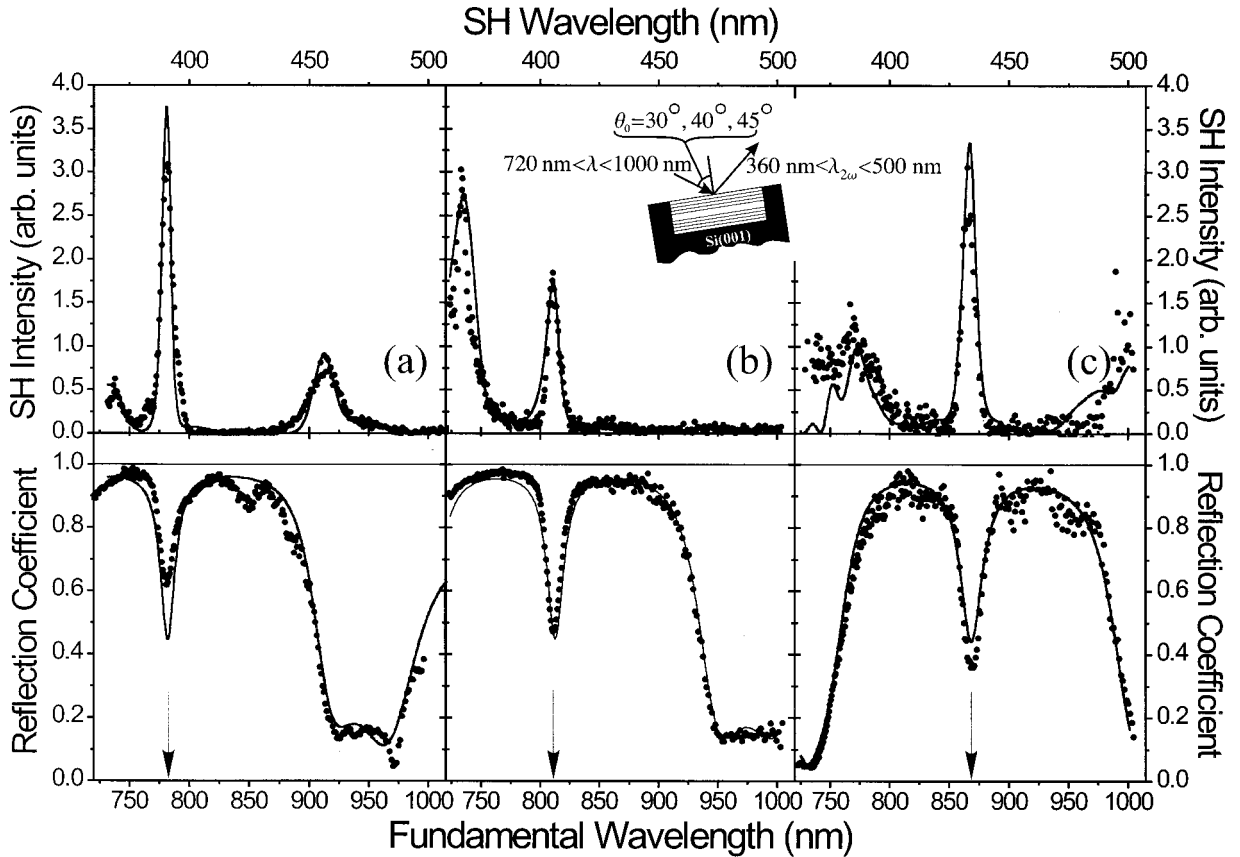


Fig. 2. Top panels:  $\omega$ -domain SH intensity spectra for MC with  $\lambda_{MC} = 945$  nm, and bottom panels: spectra of the linear reflection coefficient of the *s*-polarized fundamental wave, both measured for angles of incidence of (a)  $\theta_0 = 45^\circ$ , (b)  $\theta_0 = 40^\circ$ , and (c)  $\theta_0 = 30^\circ$ . Curves are fits of numerical-calculation results within a nonlinear optical transfer-matrix formalism to the data. The fit parameters are as follows: top, DBR-layer thickness of  $d_L \approx 240$  nm and  $d_H \approx 150$  nm; bottom, DBR-layer thicknesses of  $d_L \approx 230$  nm and  $d_H \approx 140$  nm, a cavity-layer thickness of  $d_{MC} \approx 305$  nm, and layer porosities of  $f_L = f_{MC} \approx 0.88$  and  $f_H \approx 0.77$ .

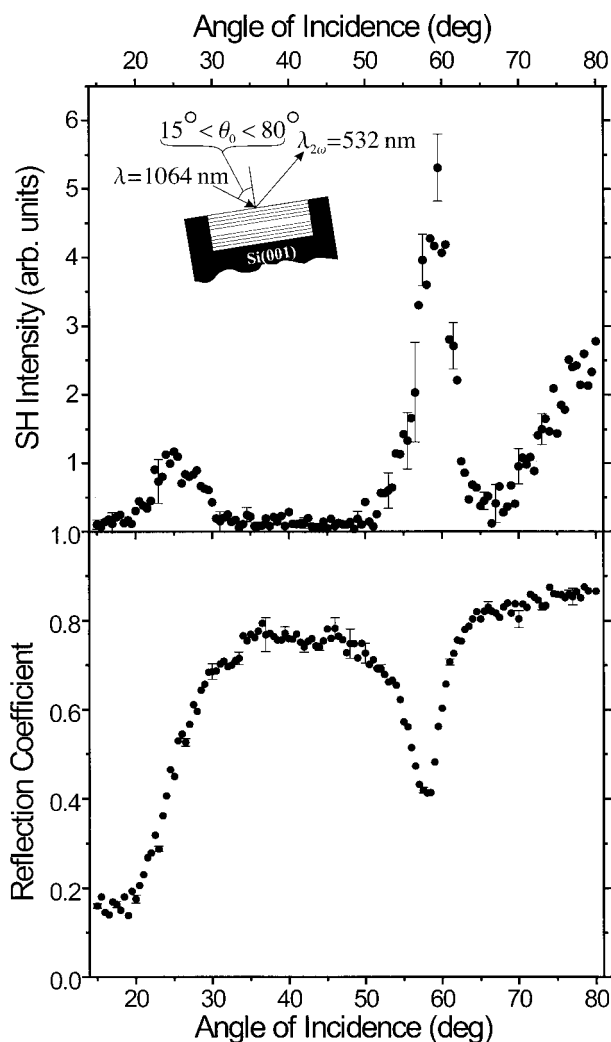


Fig. 3. Top panel:  $k$ -domain SH intensity spectra of the MC sample. Bottom panel: angular spectra of the linear reflection of the  $s$ -polarized fundamental radiation.

cleavages obtained with a scanning shear-force microscope with a piezoelectric tuning-fork detector and a scanning electron microscope. The sharp interfaces between PS layers and the high lateral quality of the MC are observed.

SHG spectroscopy in the  $\omega$  domain is measured by use of a conventional SHG setup. The output of a nanosecond-tunable optical parametric oscillator laser system operating in the range from 720 to 1050 nm with energy of approximately 10 mJ/pulse is used as the fundamental radiation. The SHG radiation is selected with an appropriate set of filters and detected with a photomultiplier tube. To normalize the SH intensity spectrum over the laser fluence and the spectral sensitivity of the detection system, we used a SH intensity reference channel with a slightly wedged Z-cut quartz plate and a detection system identical to the one in the sample channel. The SHG spectroscopy in the  $k$  domain is performed by use of 1064-nm output of a nanosecond YAG laser. The angle of incidence of the fundamental radiation is tuned from  $0^\circ$  to  $90^\circ$  in steps of  $0.5^\circ$  by use of a step-motorized

goniometer. An  $s$ -in,  $p$ -out polarization combination is used because photonic effects are more pronounced for the  $s$ -polarized fundamental radiation.

The SNOM setup is used for spatial field-distribution measurements. The SNOM tips are fabricated from a single-mode optical fiber (3M, FS-4224) by the tube-etching method. The MC cleavage that is perpendicular to the MC surface is placed onto a three-axis piezo tube scanner. The tip-sample distance is controlled by an electrical shear-force feedback system that is based on the tuning-fork technique. The sample is translated under the fixed, apertureless tip and illuminated through an external multimode fiber that is perpendicular to the surface. SNOM operates in the collection mode as the scattered light and the evanescent tail of the light confined in the sample are collected into a fiber tip and detected with a photomultiplier tube.

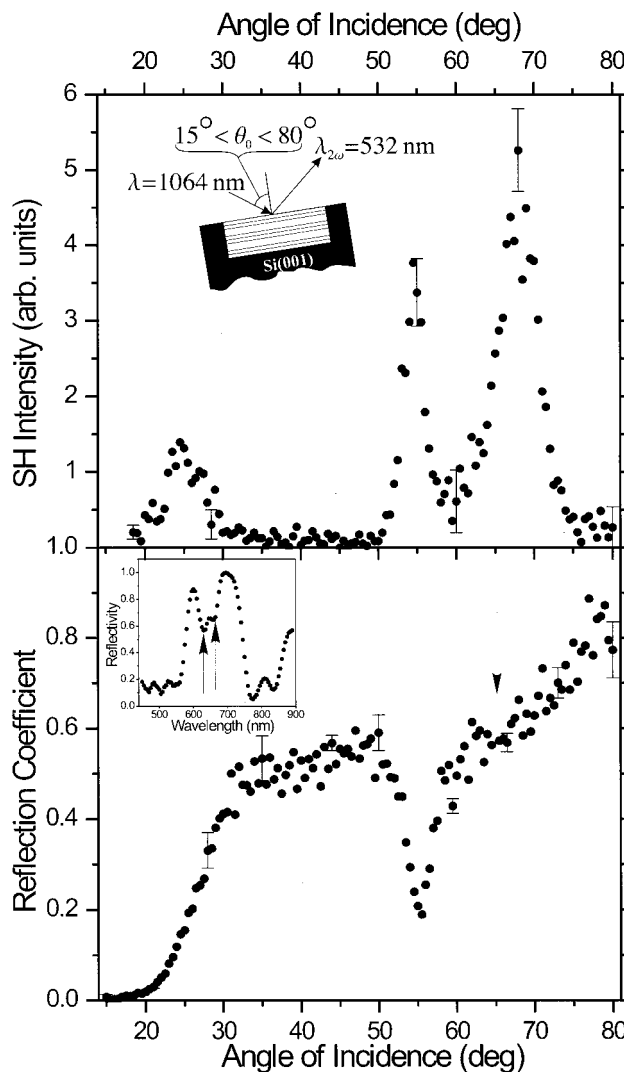


Fig. 4. Top panel:  $k$ -domain SH intensity spectrum of the coupled-MC sample. Bottom panel: angular spectrum of the linear reflection of the  $s$ -polarized fundamental radiation. Inset:  $\omega$ -domain spectrum of the linear reflection coefficient from the coupled-MC sample with  $\lambda_{MC} \approx 680$  nm at an angle of incidence of  $30^\circ$ . The arrows indicate the positions of the coupled-MC modes.

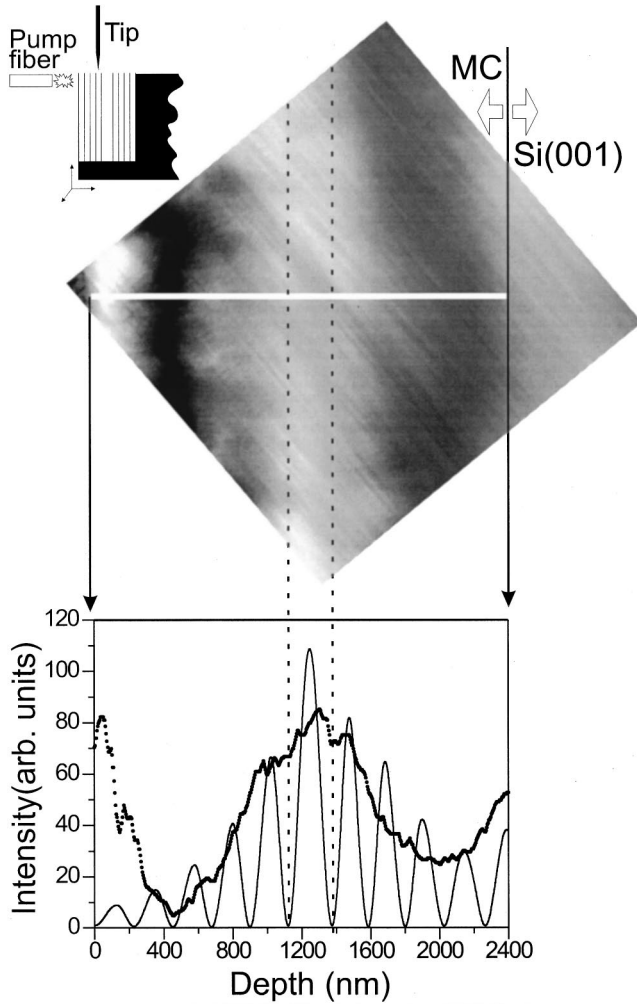


Fig. 5. Top panel: spatial distribution of the light intensity at the MC cleavage measured with SNOM. Bottom panel: cross section of the intensity distribution perpendicular to the MC surface as extracted from the SNOM image (circles) and calculated by transfer-matrix formalism (curve). The dashed lines mark the cavity layer.

### 3. EXPERIMENT

The photonic band structure or dispersion relation  $\omega(\mathbf{k})$  appears in linear and SHG spectroscopy in both the frequency and the wave-vector domains. Complete analysis requires studies of both cross sections in  $(\omega, \mathbf{k})$  space. The experimental results of SHG spectroscopy of MCs in the  $\omega$  and the  $\mathbf{k}$  domains are presented in this section. Apart from PBG and MC effects the SH intensity measured in the frequency cross section of  $(\omega, \mathbf{k})$  space is defined by spectral line shapes of linear and quadratic susceptibilities. The  $\mathbf{k}$ -domain spectrum of the SH intensity is modulated by the angular dependence of the Fresnel factors.

Figure 2 shows the SH intensity spectrum of a PS MC measured in the  $\omega$  domain at three angles of incidence:  $\theta_0 = 45^\circ, 40^\circ, 30^\circ$ . The corresponding spectra of the linear reflection coefficient of the  $s$ -polarized fundamental radiation  $R_s$  measured at the same alignment and detected by a photodiode are shown in the bottom panels.

The SH intensity  $I_{2\omega}$  is strongly enhanced, whereas the fundamental wave is in resonance with the cavity mode.  $I_{2\omega}$  is enhanced by more than 100 times in comparison with that outside the PBG. The  $Q$  factor of the SHG resonance,  $Q_{45^\circ} = \lambda_0/\Delta\lambda_0$  ( $\lambda_0$  is the resonant fundamental wavelength, and  $\Delta\lambda_0$  is full width at half-magnitude) is approximately  $67 \pm 2$ . Two other spectral features can be observed when the fundamental wavelength is tuned through the PBG edges. The SHG enhancement at these peaks is significantly smaller and does not exceed 25. The decrease in the angle of incidence leads to a monotonic red shift of all resonances, in accord with the dependence of the spectral positions of the PBG edges and the cavity mode. The mean  $Q$  factor of the SHG resonance at the MC mode appears to be mostly angle independent:  $Q = 69 \pm 4$ .

Figure 3, top panel, shows the angular dependence of the SH intensity in a MC with  $\lambda_{MC} \approx 1300$  nm. The SHG angular spectrum has a sharp resonance at  $59^\circ$  and two broad peaks at  $24^\circ$  and  $77^\circ$ . A comparison with the angular dependence of the reflection coefficient of the  $s$ -polarized wave (bottom panel) allows one to associate the first SHG resonance with the MC mode, whereas the other SHG resonance peaks with the PBG edges. The SH intensity in the MC mode achieves  $10^2$  with respect to the intensity outside the PBG. The long-wavelength edge of the PBG is not pronounced at the linear angular reflection spectrum because of the strong angular dependence of the Fresnel factors at large angles of incidence. The asymmetry of the amplitudes of the SHG peaks at the PBG edges results, in part, from the well-known angular dependence of an isotropic SHG component.

Figure 4, top panel, shows the  $\mathbf{k}$ -domain SH intensity spectrum of a coupled-MC sample with two identical spacers. The SHG angular spectrum demonstrates three resonant features: The first feature, at approximately  $25^\circ$ , is a peak at the PBG edge. The main resonances are localized in the vicinity of  $55^\circ$  and  $67^\circ$  and correspond to the SHG enhancement at the split cavity modes that is due to fundamental field localization in the vicinity of cavity spacers. The linear reflection spectrum measured in the wave-vector domain is shown in the bottom panel. The SHG resonance at  $55^\circ$  is correlated with the drop in the reflection spectrum. The second mode at  $67^\circ$  is not clearly resolved in the linear reflection spectrum because of the strong angular dependence of the Fresnel factors at large angles of incidence. However, the linear  $\omega$ -domain spectrum measured for an analogous coupled-MC sample clearly shows the mode splitting (inset of Fig. 4).

The spatial confinement of the fundamental optical field in the vicinity of the MC spacer is probed directly by means of SNOM. Figure 5 shows the resonant SNOM image measured in the MC with  $\lambda_{MC} \approx 620$  nm and pumped by the resonant 633-nm output of a cw He-Ne laser under normal incidence. The SNOM image demonstrates a broad bright strip in the vicinity of the MC spacer. The dark bands correspond to minimum intensity and coincide with the DBR. The contrast between the maximum and the minimum intensities is approximately equal to 10 and describes the field-localization degree. The bright spot at the surface area ( $z < 200$  nm) is most likely caused by sample-surface scattering of the

pump radiation. The cross section of the spatial distribution of the light intensity across the MC conforms well to the envelope of the intensity distribution calculated with transfer-matrix formalism (bottom panel). However, the fine structure of the intensity distribution with the period of the standing wave of the optical field is not resolved, although the lateral tip resolution is of order of 10 nm. This result implies that the apertureless tip detects the optical field scattered by pore edges and neighboring PS layers, decreasing the fine lateral resolution.

#### 4. MODEL

The nonlinear transfer-matrix formalism<sup>23</sup> is used for the approximation of the experimental SHG spectra both in the  $\omega$  and the  $\mathbf{k}$  domains. With this approach, first, the light propagation through the multilayer structure, taking into account multiple-reflection interference, is described. The spatial distribution of the fundamental field amplitude and the linear reflection coefficient are evaluated. Second, the spatial distribution of the quadratic polarization inside the MC is calculated. Finally, the problem of the SH wave propagation in a 1-D MC, including homogeneous and inhomogeneous wave interference, is considered.

The linear propagation of light through a multilayer structure is a standard problem of optics and can be solved by use of the transfer-matrix formalism.<sup>19</sup> Briefly, the linearly polarized plane wave  $\mathbf{E}_0^+ \exp[i(\mathbf{k}_0^\omega \mathbf{r} - \omega t)]$  is directed to the surface of the multilayer structure from the air at angle of incidence  $\theta_0$ , as shown in Fig. 6. The  $z$  axis is the normal to the layers, and  $xz$  is the plane of laser beam incidence. The spatial distribution of the optical field across the MC is evaluated as a product of transfer matrices  $\mathbf{M}_{i,j}$  for every  $ij$ th MC interface, describing the boundary conditions, and of matrices  $\Phi_j$ , describing the wave propagation in the  $j$ th MC layer (see Appendix A).

The mesoporous-silicon layers of MC are considered to be optically homogeneous layers because the typical length scale (e.g., pore size) is much smaller than the light wavelength. In this long-wavelength limit optical properties of the PS layers are characterized by the effective complex dielectric function<sup>40</sup>  $\epsilon_j$ , where  $j$  represents the number of a PS layer.  $\epsilon_j$  is calculated with the effective medium (Bruggeman) approximation<sup>36,40</sup>

$$(1 - f_j) \frac{\epsilon_{\text{Si}} - \epsilon_j}{\epsilon_{\text{Si}} + 2\epsilon_j} = f_j \frac{\epsilon_j - 1}{1 + 2\epsilon_j}, \quad (1)$$

where the porosity  $f_j$  is a measure of the air volumetric fraction of a  $j$ th PS layer,  $f_j$  is a phenomenological parameter used for calculation of  $\epsilon_j$  in the experimental spectral region on the basis of  $\epsilon_j$  values in the IR region extracted from the Fourier transform spectra of the reference PS layers, and  $\epsilon_{\text{Si}}$  is the dielectric function of crystalline silicon. For mesoporous silicon it is believed that the pore-wall material can be considered to be bulk silicon. Thus the spectral dependence of complex  $\epsilon_{\text{Si}}$  determines the spectral behavior of  $\epsilon_j$ .

To obtain the spatial distribution of the quadratic polarization across MC by means of a known spatial distri-

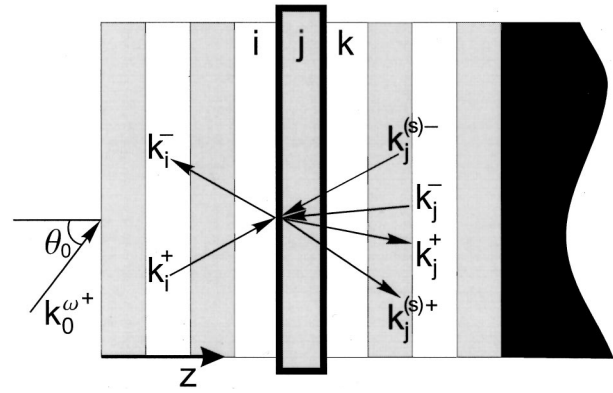


Fig. 6. Schematic of a multilayer nonlinear medium. The wave vectors of forward- and backward-propagating homogeneous SH waves in the  $i$ th and the  $j$ th layers and of inhomogeneous SH waves in the  $j$ th layer are shown.

bution of the fundamental field requires first that a model of the quadratic susceptibility tensor of the MC,  $\hat{\chi}^{(2)}$ , be defined. The types of nonlinear sources in PS (electric dipole or quadrupole) and the localization (the PS surface or bulk) are discussed extensively in the literature.<sup>41,42</sup> The dipole contribution to quadratic polarization is induced at the PS interfaces as well as at the big area of the inner pore surfaces, where the inversion symmetry of bulk silicon is necessarily broken. The quadrupole term can be expected from the bulk of silicon nanocrystals forming PS. However, the quadrupole term should possess bulk-silicon symmetry and demonstrate fourfold symmetry in the SHG azimuthal anisotropic measurements. On the other hand, the experiment shows the independence of the SH intensity from the azimuthal angle of the PS MC and allows us to consider the PS layers constituting MC as isotropic in the plane. Thus for the present model the mechanism of dipole nonlinear sources uniformly distributed over the bulk of each PS layer is taken. The corresponding symmetry group  $\infty m$  describes the presence of an infinite number of symmetry planes containing  $z$  axes that are perpendicular to the surface and imposed by the etching geometry.

The effective dipole quadratic polarization inside the  $j$ th PS layer is given by

$$\mathbf{P}_j^{2\omega}(z) = \hat{\chi}_j^{(2)} : \mathbf{E}_j^\omega(z) \mathbf{E}_j^\omega(z), \quad (2)$$

with three nonzero independent components of the second-order susceptibility tensor of the  $j$ th layer,  $\hat{\chi}_j^{(2)}$ :

$$\begin{aligned} \chi_1 &\equiv \chi_{xxz} = \chi_{yzy} = \chi_{xxz} = \chi_{yyz}, \\ \chi_2 &\equiv \chi_{zxx} = \chi_{zyy}, \\ \chi_3 &\equiv \chi_{zzz}. \end{aligned} \quad (3)$$

Then the modules of the  $s$ - and the  $p$ -polarized quadratic polarization vectors  $\mathbf{P}_s$  and  $\mathbf{P}_p$ , respectively, can be written as

$$\begin{aligned} P_s(z) &= 2\chi_1 E_s^\omega(z) E_p^\omega(z) \sin \theta, \\ P_p(z) &= (P_\perp^2 + P_\parallel^2)^{1/2}, \end{aligned} \quad (4)$$

where  $\mathbf{E}_s^\omega$  and  $\mathbf{E}_p^\omega$  are  $s$ - and  $p$ -polarized fundamental waves, respectively, and all quantities relate to the  $j$ th PS

layer.  $\mathbf{P}_\perp(z)$  and  $\mathbf{P}_\parallel(z)$  are perpendicular and parallel to the wave vector  $\mathbf{k}_s = 2\mathbf{k}_j^\omega$  components of  $\mathbf{P}_p$ :

$$\begin{aligned} P_\perp &= \chi_1(E_p^\omega)^2 \sin 2\theta \cos \theta - \chi_2(E_p^\omega)^2 \cos^2 \theta \sin \theta \\ &\quad - \chi_2(E_s^\omega)^2 \sin \theta - \chi_3(E_p^\omega)^2 \sin^3 \theta, \\ P_\parallel &= \chi_1(E_p^\omega)^2 \sin 2\theta \sin \theta + \chi_2(E_p^\omega)^2 \cos^3 \theta \\ &\quad + \chi_2(E_s^\omega)^2 \cos \theta + \chi_3(E_p^\omega)^2 \sin^2 \theta \cos \theta. \end{aligned} \quad (5)$$

Multiple reflections of the fundamental field are correctly taken into account in the complex quantities  $\mathbf{P}_s(z)$  and  $\mathbf{P}_p(z)$ .

The spectral dependence of the PS quadratic susceptibility  $\hat{\chi}_j^{(2)}$  can be modeled with the same spectral line shape as that of crystalline silicon because the quantum confinement is assumed to be negligible in mesoporous silicon with a pore size of the order of tens of nanometers. For the SH photon energies of less than 3.45 eV used in the experiment, two-photon resonance is taken with the Lorentzian line shape corresponding to the  $E_0'/E_1$  critical point of the crystalline silicon band structure.<sup>43</sup> To take into account the volume fraction of silicon in a PS layer, we normalize the quadratic susceptibility by porosity:

$$\hat{\chi}_j^{(2)} = [a - b/(-\Omega + 2\omega + i\Gamma)](1 - f_j). \quad (6)$$

Here the resonant amplitude  $b$  and the spectral background  $a \ll b$  are adjustable parameters, the central energy is  $\Omega \approx 3.35$  eV, and the broadening is  $\Gamma \approx 0.1$  eV.

The quadratic polarization vector  $\mathbf{P}_j^{2\omega}$  given by

$$\mathbf{P}_j^{2\omega} = \mathbf{P}_s + \mathbf{P}_\perp + \mathbf{P}_\parallel \quad (7)$$

generates the inhomogeneous SH wave in the  $j$ th layer<sup>44</sup>:

$$\mathbf{E}^{(s)} = \frac{4\pi}{\epsilon_j(\omega) - \epsilon_j(2\omega)} (\mathbf{P}_s + \mathbf{P}_\perp) - \frac{4\pi}{\epsilon_j(2\omega)} \mathbf{P}_\parallel. \quad (8)$$

$\mathbf{P}_j^{2\omega}$  of the  $j$ th PS layer is independent of other layers if the fundamental wave depletion is negligible. Then the problem of interference of the homogeneous and the inhomogeneous SH waves in the nonlinear multilayer structure can be transformed into a problem of generation and propagation of the SH wave from the single  $j$ th nonlinear layer that is incorporated into a stack of linear slabs. The boundary conditions at both surfaces of the  $j$ th layer take into account the interference of the homogeneous SH wave  $\mathbf{E}_j$  propagating inside the  $j$ th layer with the inhomogeneous SH wave  $\mathbf{E}^{(s)}$  generated there.<sup>44</sup> These conditions are described by two additional matrices,  $\mathbf{M}_i^{(s)}$  and  $\Phi^{(s)}$ , by analogy to the formalism described in Ref. 23 for third-harmonic generation in a multilayer structure. The matrices reflect the simple fact that the inhomogeneous SH wave propagates in the direction determined by the linear dispersion at the fundamental wavelength. Outside the  $j$ th layer the homogeneous SH wave is multiply reflected in the linear multilayer structure, producing the complex partial SH field in air  $\mathbf{E}_{0,j}$ . The total SH field generated in the MC is given by the summation of such complex partial contributions from all layers. The derivation of equations for the calculation of  $\mathbf{E}_{0,j}$  is given in detail in Appendix A.

The approach of the complex partial SH fields generated in every MC layer inherently takes into account the

phase-matching effects because the phase of the  $\mathbf{E}_{0,j}$  field contains all the phase shifts produced by the interference of backward- and forward-propagating waves at both the fundamental and the SH wavelengths.

## 5. DISCUSSION

### A. Numerical Results

For numerical simulations an ideal MC sample similar to the one studied in the SHG spectroscopy experiments in the  $\omega$  domain (Fig. 2) is considered. The MC is assumed to consist of a top DBR with 5.5 pairs of layers with an exact thickness of  $\lambda_{MC}/4$ , a  $\lambda_{MC}/2$ -thick cavity spacer, and

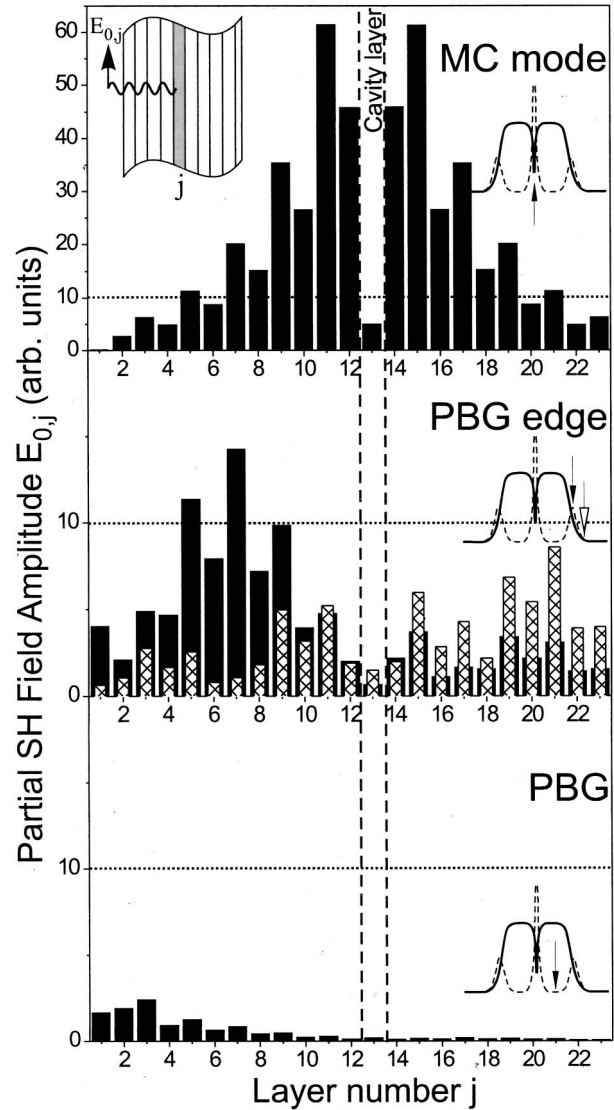


Fig. 7. Amplitudes of outgoing partial SH fields  $|\mathbf{E}_{0,j}|$  generated in every  $j$ th layer of the MC plotted as functions of the layer number calculated for fundamental wavelengths at the cavity mode (top panel), near the PBG edge at the spectral position of the SHG peak (filled bars in middle panel) and outside the PBG (crosshatched bars in middle panel), and inside the PBG (bottom panel). The spectral positions are marked at the sketched linear reflection and SHG spectra in the insets. The dashed lines indicate the cavity spacer, and the topmost layer is layer 1. Details of the ideal MC sample used for calculation are given in the text.

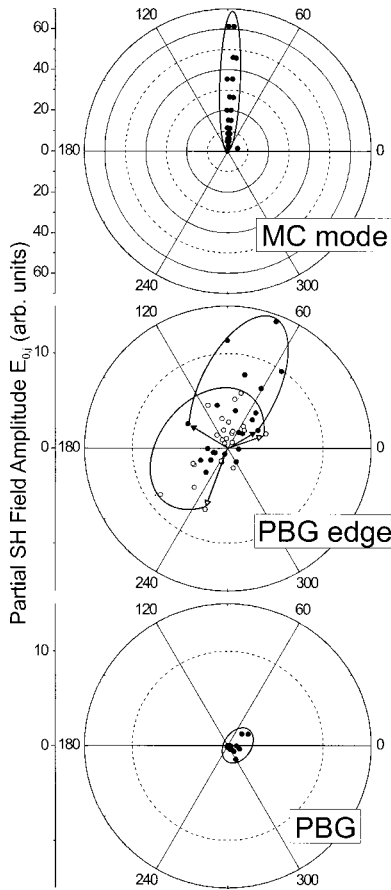


Fig. 8. Partial SH contributions  $\mathbf{E}_{0,j}$  presented at the complex plane and calculated for the fundamental wavelength at the cavity mode (top panel), near the PBG edge (middle panel), and inside the PBG (bottom panel).

a bottom DBR with 5 pairs of  $\lambda_{MC}/4$ -thick layers. The top DBR is assumed to be covered by an additional  $\lambda_{MC}/2$ -thick layer. The refractive indices of the layers are taken to be  $n_L = n_{MC} = 1.17$  and  $n_H = 1.41$ , with  $\lambda_{MC} \approx 960$  nm. The *s*-polarized fundamental radiation is assumed to be directed at an angle of incidence of  $\theta_0 = 45^\circ$ . Dispersion and absorption are neglected. The SH field is calculated for four specific wavelengths of the linear reflection spectrum, which are shown schematically in the insets of Fig. 7, namely, at the cavity mode, at the long-wavelength PBG edge, at the point with minimal reflectivity near the PBG, and inside the PBG with maximum reflectivity achieved.

Figure 7 shows the amplitudes of the partial SH fields  $|\mathbf{E}_{0,j}|$  plotted as functions of the layer number *j* calculated for marked specific points of the photonic band structure. The dependences clearly demonstrate the role of the fundamental-field localization in the enhancement of the SHG response of 1-D MCs. For the cavity mode (top panel, Fig. 7),  $|\mathbf{E}_{0,j}|$  are strongly enhanced, especially in the vicinity of the spacer, and are almost 1 order of magnitude larger than the partial SH fields calculated for the PBG edge, which are depicted in the middle panel of Fig. 7. The largest enhancement of the SH field is produced in the DBR layers near the MC spacer. These results are consistent with the enhancement of the fundamental field in the vicinity of the cavity spacer in which the funda-

mental field is increased by a factor of approximately 5 in comparison with the incoming field. At the MC mode, the spatial distribution of the fundamental field across the spacer is symmetric, and half of the fundamental wavelength is exactly equal to the optical thickness of the MC spacer. The SH field from the left-hand half of the spacer destructively interferes with the SH contribution from the right-hand half. In the extreme case of  $n(\omega) = n(2\omega)$  the SH signal from the MC spacer tends to zero. At the PBG edge (middle panel of Fig. 7)  $|\mathbf{E}_{0,j}|$  are slightly enhanced as a result of the homogeneous increase of the fundamental field inside the MC, which is consistent with previous SHG studies.<sup>16,25</sup> The bottom panel of Fig. 7 shows the SH fields  $|\mathbf{E}_{0,j}|$  calculated for the fundamental wavelength inside the PBG.  $|\mathbf{E}_{0,j}|$  are almost negligible and exponentially decay deep into the MC, in accord with the fundamental field decay for forbidden states inside the PBG.

Figure 8 shows the same partial SH field contributions  $\mathbf{E}_{0,j}$  at complex planes and demonstrates the role of phase matching in SHG enhancement at the cavity mode and the PBG edges. For the case of the MC mode depicted in the top panel most of the  $\mathbf{E}_{0,j}$  fields have phases in the narrow angular region with a width of approximately  $10^\circ$ . This outcome means that the  $\mathbf{E}_{0,j}$  contributions interfere constructively, fulfilling phase-matching conditions, and produce enhancement of the total SH field, strengthening the fundamental field localization effect.

For SHG enhancement at the PBG edge phase matching is even more important. The middle panel of Fig. 8 shows polar diagrams for the fundamental wavelengths near the PBG edge. All significant partial SH field contributions for the SHG maximum (filled circles) interfere constructively because the phase shifts between them do not exceed  $90^\circ$ . Meanwhile, the phases of the  $\mathbf{E}_{0,j}$  contributions for the SHG minimum (open circles) are spread almost homogeneously, and the SH fields from the top DBR destructively interfere with those from the bottom one. At the same time the amplitudes of  $\mathbf{E}_{0,j}$  for the SHG maximum at the PBG edge are comparable with those for the SHG minimum.

## B. Discussion and Comparison with the Experiment

The experimental  $\omega$ -domain SH intensity and linear reflection spectra (Fig. 2) are fitted by use of the nonlinear optical transfer-matrix formalism described in Section 4. First, linear reflection spectra for all three angles of incidence are fitted simultaneously by the least-squares procedure. The adjustable parameters are the thicknesses of the low-refractive-index and the high-refractive-index PS layers,  $d_L$  and  $d_H$ , and their refractive indices,  $n_L$  and  $n_H$ , respectively. The dispersion of  $n_L$  and  $n_H$  at both the fundamental and the SH wavelengths is determined by Eq. (1) by use of the dispersion of bulk silicon and the corresponding porosities  $f_L$  and  $f_H$ . Then the SH intensity spectra for all three angles of incidence are simultaneously fitted with the fixed layer thickness and dispersion. The adjustable parameters for this approximation are the parameters of the spectral profile of the effective quadratic susceptibility of the PS layers given by Eq. (6). The ratio of the resonant amplitude *b* over the spectral background *a* appears to be  $b/a \approx 8.5$ . The results of the

approximation shown in Fig. 2 by the curves fit the experimental data well and prove the presence of both SHG enhancement mechanisms discussed above. The MC spacer thickness  $d_{MC}$  is smaller than  $\lambda_{MC}/2$  expected. Other parameters are in a good agreement with the values expected from the independent calibration of the PS-etching rate.

For comparison the observed MC enhancement, SHG spectroscopy of two reference samples was performed. The first sample is the single PS layer with a porosity of  $f \approx 0.7$  and a refractive index of  $n \approx 1.65$  at 1064 nm. The PS-layer thickness is approximately  $2 \mu\text{m}$ , which is close to the total thickness of studied MCs. The SHG spectroscopy of such single PS layers allows us to determine the influence of the buried MC interfaces on the SHG enhancement. The second reference sample is the natively oxidized Si (001) wafer, which is used as a substrate for the PS MCs. The Si (001) layer was chosen because SHG from the silicon surface does not influence the phase-matching mechanism, and the SH intensity is determined directly by the corresponding components of the quadratic susceptibility tensor.

Figure 9, top panel, shows the SHG spectrum of the reference PS layer measured in the wave-vector domain. The wide maximum in the SH intensity at  $\theta_0 = 50^\circ$  and the oscillation in the reflection coefficient spectra (bottom panel of Fig. 9) indicate that the SHG signal is generated from the PS bulk. Because of the high silicon refractive index, the reflection of the fundamental wave from the

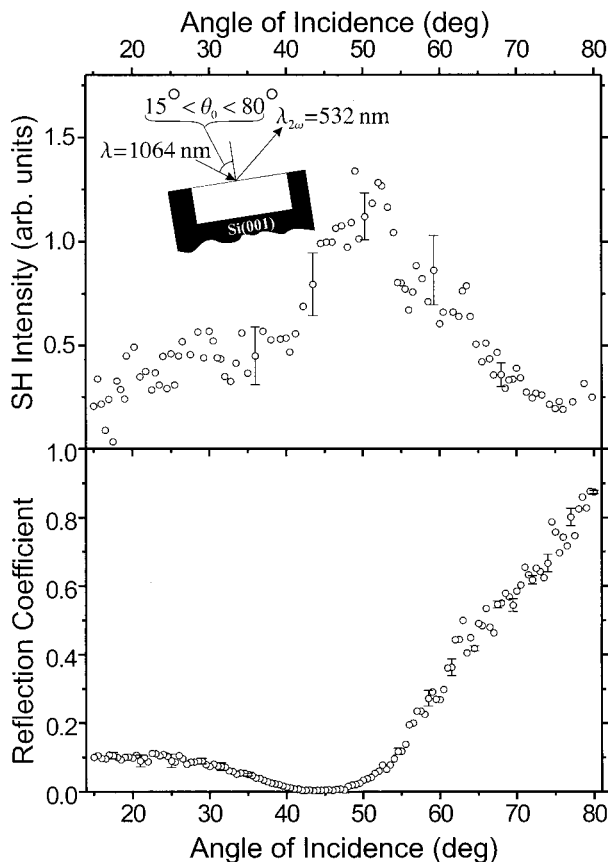


Fig. 9. Top panel:  $\mathbf{k}$ -domain SH intensity spectra of the reference PS slab. Bottom panel: angular spectra of linear reflection of the  $s$ -polarized fundamental radiation.

PS-layer–silicon-substrate interface is large, and the PS layer acts as a Fabry–Perot filter. Its  $Q$  factor is substantially smaller than that of the PS MC; therefore the SHG peak for the reference PS layer is approximately 4 times smaller and 4 times wider (FWHM) in comparison with the SHG resonance at the MC mode shown in Fig. 3. An additional cause of the SHG increase in the single PS layer is the fact that the coherence length for the PS with a porosity of  $f \approx 0.7$  is estimated to be  $\sim 3 \mu\text{m}$  at the fundamental wavelength of 1064 nm. For the Si (001) surface the angular SHG spectrum is measured in the maximum of the rotational azimuthal anisotropy in a  $p$ -in,  $p$ -out polarization combination. The dependence demonstrates the shape that is conventional for the azimuthal isotropic SHG component<sup>45</sup> with the maximum at approximately  $60^\circ$  of incidence. The maximal SH intensity is at least 150 times smaller than that achieved in the MC.

The internal reference for normalization of the MC SHG enhancement would be the SH intensity generated in the same MC but for the off-resonant fundamental wavelength outside the PBG. In this spectral region, the MC is transparent for the fundamental field, and there is no suppression of the SHG signal such as takes place inside the PBG, where the fundamental field exponentially decays. On the other hand, there is no effect of fundamental field confinement leading to SHG enhancement. Moreover, the partial SHG contributions from individual layers of the MC are not in phase as long as their constructive interference provides the phase-matching mechanism of enhancement. The SH intensity averaged over the slight interference oscillations outside the PBG is taken as the reference SHG signal. The MC enhancement obtained for a MC with  $\lambda_{MC} \approx 945 \text{ nm}$  [ $\theta_0 = 45^\circ$ , Fig. 2(a)] relative to the off-resonant SH intensity averaged over the fundamental wavelength interval from 925 to 1025 nm appears to be approximately 130 times.

## 6. CONCLUSIONS

In summary the SHG spectra of single and coupled photonic-crystal MCs have been experimentally studied in both the frequency and the wave-vector domains. The photonic crystals (DBRs) forming the cavity mirrors were fabricated from alternating quarter-wavelength-thick layers of mesoporous silicon with differing porosities. The cavity spacer was a half-wavelength-thick mesoporous silicon layer. Resonance enhancement of the SH intensity has been observed in the case of the fundamental field resonance with the cavity mode. The SHG enhancement achieved was 130 times relative to the off-resonant SH intensity measured for the fundamental field outside the PBG and more than 200 times relative to the SHG signal from the Si (001) surface.

From a comparison of the experimental results with numerical simulations within the nonlinear transfer-matrix formalism two mechanisms have been shown to be responsible for this SHG enhancement: (i) the high SHG efficiency resulting from the spatial confinement of the

fundamental field inside the cavity spacer, and (ii) the constructive interference of the SH fields generated in DBR layers near the spacer.

Additional SHG enhancement has been observed in the MC spectra at the PBG edge. This SHG enhancement is analogous to the SH intensity increase conventionally observed at the PBG edges of photonic crystals and is caused by combined effects of phase matching and the uniform enhancement of the fundamental field in the DBR.

Finally, the angular spectrum of the SHG response of two identical MCs coupled through an additional DBR has been studied. Two SHG resonances attributed to split modes of identical coupled cavities have been observed. The amplitudes of the SHG resonances have been shown to be dependent on the parameters of the intermediate DBR that separates two cavity spacers.

## APPENDIX A

In this appendix the expressions for the reflection coefficient and the SH intensity spectra of 1-D MCs are derived by use of the nonlinear optical transfer-matrix formalism. Wave propagation through a linear multilayer structure can be evaluated with the well-known optical transfer-matrix method.<sup>19</sup> SHG in a single nonlinear slab sandwiched between two linear dielectrics was described in Ref. 44. The general case of the nonlinear optical response of a multilayer structure was discussed in Ref. 23 for third-harmonic generation.

Let us consider a linearly polarized fundamental plane wave with the wave vector  $\mathbf{k}_0^\omega$  directed onto the surface of a multilayer structure at an angle of incidence  $\theta_0$ , as sketched in Fig. 6. The fundamental field inside the  $j$ th MC layer is the superposition of forward- and backward-propagating waves

$$\begin{aligned} \mathbf{E}_j^\omega(z, t) = & \mathbf{E}_j^+ \exp[+ik_{z,j}^\omega(z - d_{ij}) + (ik_x^\omega x - i\omega t)] \\ & + \mathbf{E}_j^- \exp[-ik_{z,j}^\omega(z - d_{ij}) \\ & + (ik_x^\omega x - i\omega t)], \end{aligned} \quad (\text{A1})$$

where the tangential component of the wave vector  $k_x^\omega = |\mathbf{k}_j^\omega| \sin \theta_j$  remains constant across the structure, the normal wave-vector component is  $k_{z,j}^\omega = |\mathbf{k}_j^\omega| \cos \theta_j$ , and  $d_{ij}$  is the  $z$  coordinate of the  $ij$ th interface.  $\theta_j$  is the angle of incidence of the fundamental wave inside the  $j$ th layer. As a result of the translation symmetry in the  $xy$  plane and the steady-state case, the term  $\exp(ik_x^\omega x - i\omega t)$  is omitted. The fundamental radiation in the  $j$ th and the  $i$ th layers near the  $ij$ th interface are given by  $\mathbf{E}_j^\omega = \mathbf{E}_j^+ + \mathbf{E}_j^-$  and  $\mathbf{E}_i^\omega = \mathbf{E}_i^+ + \mathbf{E}_i^-$ . The relation between  $\mathbf{E}_i^\omega$  and  $\mathbf{E}_j^\omega$  is determined by the boundary conditions. The continuity of the tangential components of the electric and the magnetic fields leads to a system of two characteristic equations. Solution of this system can be written as a matrix equation

$$\begin{bmatrix} \mathbf{E}_i^+ \\ \mathbf{E}_i^- \end{bmatrix} = \begin{bmatrix} 1/t_{ij} & r_{ij}/t_{ij} \\ r_{ij}/t_{ij} & 1/t_{ij} \end{bmatrix} \begin{bmatrix} \mathbf{E}_j^+ \\ \mathbf{E}_j^- \end{bmatrix}, \quad (\text{A2})$$

where  $t_{ij}$  and  $r_{ij}$  are Fresnel transmission and reflection coefficients for the light incident from the  $i$ th layer. Denote the two-component vector as

$$\begin{bmatrix} \mathbf{E}_j^+ \\ \mathbf{E}_j^- \end{bmatrix} = \mathbf{E}_j \quad (\text{A3})$$

and the matrix as

$$\begin{bmatrix} 1/t_{ij} & r_{ij}/t_{ij} \\ r_{ij}/t_{ij} & 1/t_{ij} \end{bmatrix} = \mathbf{M}_{ij}. \quad (\text{A4})$$

The matrix  $\mathbf{M}_{ij}$  is the transfer matrix for the  $ij$ th interface. The fundamental fields at points  $z_j$  and  $z_j + \zeta$ , both located inside the  $j$ th layer, are connected as

$$\mathbf{E}_j(z_j + \zeta) = \Phi_j(\zeta) \mathbf{E}_j(z_j) \quad (\text{A5})$$

by means of the propagation matrix

$$\Phi_j(\zeta) = \begin{bmatrix} \exp(ik_{z,j}^\omega \zeta) & 0 \\ 0 & \exp(-ik_{z,j}^\omega \zeta) \end{bmatrix}. \quad (\text{A6})$$

The total transfer matrix from the air (the zeroth layer) to the silicon substrate (the  $l$ th layer) has the form

$$\mathbf{T} = \mathbf{M}_{l(l-1)} \Phi_{l-1} \cdots \mathbf{M}_{10}, \quad (\text{A7})$$

where  $\Phi_m = \Phi_m(d_m)$  and  $d_m$  is the thickness of the  $m$ th layer. The reflection coefficient is  $R = -T_{21}/T_{22}$ , where  $T_{21}$  and  $T_{22}$  are matrix elements of  $\mathbf{T}$ . If the amplitude of the incident fundamental wave is a unit, the two-component vector of the fundamental field in air is  $\mathbf{E}_0^\omega = \{1, R\}$ , and the spatial distribution of the fundamental wave inside the MC is the following:

$$\begin{aligned} \mathbf{E}_j^\omega(z) = & \mathbf{T}_j(z) \mathbf{E}_0^\omega \\ = & \begin{bmatrix} \exp(ik_{z,j}^\omega z) & 0 \\ 0 & \exp(-ik_{z,j}^\omega z) \end{bmatrix} \\ & \times \mathbf{M}_{j(j-1)} \Phi_{j-1} \cdots \mathbf{M}_{10} \begin{bmatrix} 1 \\ R \end{bmatrix}. \end{aligned} \quad (\text{A8})$$

To obtain the spatial distribution of the quadratic polarization  $\mathbf{P}_j^{2\omega}(z)$ , we convolute the second-order susceptibility with the distribution of the fundamental field  $\mathbf{E}_j^\omega(z)$ . The inhomogeneous SH wave  $\mathbf{E}^{(s)}$ , which is associated with  $\mathbf{P}_j^{2\omega}(z)$ , is given by Eq. (8). The problem of propagation of both the homogeneous and the inhomogeneous SH waves in a multilayer structure can be reduced to that in a single nonlinear layer sandwiched between two stacks of linear slabs if the depletion of the fundamental field can be neglected. The interference of the homogeneous  $\mathbf{E}_j$  and the inhomogeneous  $\mathbf{E}^{(s)}$  SH waves inside nonlinear slab is taken into account by means of boundary conditions on the slab interfaces. If we assume that the  $j$ th layer has only nonzero second-order susceptibility  $\hat{\chi}_j^{(2)}$ , boundary conditions at the  $ij$ th and  $jk$ th interfaces for the SH waves in the matrix method have the form

$$\mathbf{E}_i = \mathbf{M}_{ij} \mathbf{E}_j + \mathbf{M}_i^{(s)} \mathbf{E}^{(s)},$$

$$\mathbf{M}_{kj} \Phi_j \mathbf{E}_j + \mathbf{M}_k^{(s)} \Phi_k \mathbf{E}^{(s)} = \mathbf{E}_k. \quad (\text{A9})$$

Matrices  $\mathbf{M}_i^{(s)}$ ,  $\mathbf{M}_k^{(s)}$ , and  $\Phi^{(s)}$  are organized as matrices  $\mathbf{M}_{ij}$ ,  $\mathbf{M}_{kj}$ , and  $\Phi_j$ , respectively, related to the homogeneous SH wave, but all subscripts  $j$  are replaced with su-

perscripts ( $s$ ). Superscript ( $s$ ) denotes quantities related to the inhomogeneous SH wave such as  $\mathbf{k}_s = 2\mathbf{k}_j^\omega$ ,  $\theta_s = \theta_j$ , and  $\epsilon_s = \epsilon_j(\omega)$ . The simultaneous solution of Eq. (A9) gives the SH field in the  $k$ th layer

$$\mathbf{E}_k = \mathbf{M}_{kj}\Phi_j(\mathbf{M}_{ji}\mathbf{E}_i + \mathbf{S}_j), \quad (\text{A10})$$

where

$$\mathbf{S}_j = [\bar{\Phi}_j\mathbf{M}_j^{(s)}\Phi^{(s)} - \mathbf{M}_j^{(s)}]\mathbf{E}^{(s)} \quad (\text{A11})$$

and matrix  $\bar{\Phi}_j$  is the inverse of  $\Phi_j$ . Expression (A10) gives the SH field in the  $k$ th layer as a superposition of the SH wave, transmitted from the  $i$ th layer, and the SH wave, generated by nonlinear sources in the  $j$ th layer. The vector  $\mathbf{S}_j$  reflects interference of the homogeneous and the inhomogeneous SH waves in the  $j$ th nonlinear layer. Let  $\mathbf{E}_{l,j} = \{E_{l,j}^+, 0\}$  and  $\mathbf{E}_{0,j} = \{0, E_{0,j}^-\}$  denote the partial contributions of the  $j$ th layer to the SH field in the  $l$ th and the zeroth layers. Then Eq. (A10) can be written as follows:

$$\mathbf{R}_{ji}\mathbf{E}_{l,j} - \mathbf{L}_{j0}\mathbf{E}_{0,j} = \mathbf{S}_j. \quad (\text{A12})$$

Matrices

$$\mathbf{R}_{ji} \equiv \bar{\Phi}_j\mathbf{M}_{jk}\bar{\Phi}_k \cdots \bar{\Phi}_{(l-1)}\mathbf{M}_{(l-1)l}, \quad (\text{A13})$$

$$\mathbf{L}_{j0} \equiv \mathbf{M}_{ji}\Phi_i\mathbf{M}_{i(i-1)} \cdots \Phi_1\mathbf{M}_{10} \quad (\text{A14})$$

describe the propagation of the homogeneous SH waves from the  $l$ th (substrate) and the zeroth (air) layers to the  $j$ th layer. Therefore the calculated  $\mathbf{S}_j$  vector allows us to find the contribution from the  $j$ th nonlinear layer to the reflected SH wave in air. Finally, the total SH wave is a summation of the partial contributions  $\mathbf{E}_{0,j}$  over all layers.

## ACKNOWLEDGMENTS

The authors are pleased to acknowledge D. V. Kazantsev and D. Schuhmacher for help in the SNOM and the SHG experiments. This study was supported by the Russian Foundation for Basic Research (RFBR) and the Deutsche Forschungsgemeinschaft (DFG): DFG grant 436 RUS 113/640/0-1, RFBR grants 01-02-16746, 01-02-17524, and 01-02-04018, special grant for Leading Russian Science Schools 00-15-96555, and International Association for the promotion of cooperation with scientists from the New Independent States of the former Soviet Union (INTAS) grant YSF-2001/1-160. N. Otha acknowledges the Obuchi Fellowship Program (Japan–Russia Youth Exchange Center).

O. A. Aktsipetrov's e-mail address is aktsip@shg.ru; the URL is <http://www.shg.ru>.

## REFERENCES

1. A. Imhof, W. Vos, R. Sprik, and A. Lagendijk, "Large dispersive effects near the band edges of photonic crystals," *Phys. Rev. Lett.* **83**, 2942–2945 (1999).
2. K. Sakoda, *Optical Properties of Photonic Crystals* (Springer-Verlag, Berlin, 2001).
3. E. Yablonovitch, "Inhibited spontaneous emission in solid-state physics and electronics," *Phys. Rev. Lett.* **58**, 2059–2062 (1987).
4. A. Ortigosa-Blanch, J. C. Knight, W. J. Wadsworth, J. Arriaga, B. J. Managan, T. A. Birks, and P. St. J. Russell, "Highly birefringent photonic-crystal fibers," *Opt. Lett.* **25**, 1325–1327 (2000).
5. F. Genereux, S. W. Leonard, H. M. van Driel, A. Birner, and U. Gösele, "Large birefringence in two-dimensional silicon photonic crystals," *Phys. Rev. B* **63**, 161101(R)–161104(R) (2001).
6. M. Scalora, J. P. Dowling, C. M. Bowden, and M. J. Bloemer, "Optical limiting and switching of ultrashort pulses in nonlinear photonic band gap materials," *Phys. Rev. Lett.* **73**, 1368–1371 (1994).
7. W. Chen and D. L. Mills, "Gap solitons and the nonlinear optical response of superlattices," *Phys. Rev. Lett.* **58**, 160–163 (1987).
8. J. A. Armstrong, N. Bloembergen, J. Ducuing, and P. S. Pershan, "Interactions between light waves in a nonlinear dielectric," *Phys. Rev.* **127**, 1918–1939 (1962).
9. V. Berger, "Nonlinear photonic crystals," *Phys. Rev. Lett.* **81**, 4136–4139 (1998).
10. S. J. B. Yoo, C. Caneau, R. Bhat, M. A. Koza, A. Rajhel, and N. Antoniadis, "Wavelength conversion by difference frequency generation in AlGaAs waveguides with periodic domain inversion achieved by wafer bonding," *Appl. Phys. Lett.* **68**, 2609–2611 (1996).
11. L. E. Myers, R. C. Eckardt, M. M. Fejer, R. L. Byer, W. R. Bosenberg, and J. W. Pierce, "Quasi-phase-matched optical parametric oscillators in bulk periodically poled LiNbO<sub>3</sub>," *J. Opt. Soc. Am. B* **12**, 2102–2116 (1995).
12. N. G. R. Broderick, G. W. Ross, H. L. Offerhaus, D. J. Richardson, and D. C. Hanna, "Hexagonally poled lithium niobate: a two-dimensional nonlinear photonic crystal," *Phys. Rev. Lett.* **84**, 4345–4348 (2000).
13. N. Bloembergen and J. Sievers, "Nonlinear optical properties of periodic laminar structures," *Appl. Phys. Lett.* **17**, 483–486 (1970).
14. J. P. van der Ziel and M. Ilegems, "Optical second harmonic generation in periodic multilayer GaAs–Al<sub>0.3</sub>Ga<sub>0.7</sub>As structures," *Appl. Phys. Lett.* **28**, 437–439 (1976).
15. Y. Dumeige, P. Vidakovic, S. Sauvage, I. Sagnes, J. A. Levenson, C. Sibilias, M. Centini, G. D'Aguanno, and M. Scalora, "Enhancement of second-harmonic generation in a one-dimensional semiconductor photonic band gap," *Appl. Phys. Lett.* **78**, 3021–3023 (2001).
16. A. V. Balakin, V. A. Bushuev, N. I. Koroteev, B. I. Mantsyzov, I. A. Ozheredov, A. P. Shkurinov, D. Boucher, and P. Masselin, "Enhancement of second-harmonic generation with femtosecond laser pulses near the photonic band edge for different polarizations of incident light," *Opt. Lett.* **24**, 793–795 (1999).
17. L. A. Golovan, A. M. Zheltikov, P. K. Kashkarov, N. I. Koroteev, M. G. Lisachenko, A. N. Naumov, D. A. Sidorov-Biryukov, V. Yu. Timoshenko, and A. B. Fedotov, "Generation of the second optical harmonic in porous-silicon-based structures with a photonic band gap," *JETP Lett.* **69**, 300–305 (1999) [*Pis'ma Zh. Eksp. Teor. Fiz.* **69**, 274–279 (1999)].
18. T. V. Dolgova, A. I. Maidikovskiy, M. G. Martemyanov, G. Marowsky, G. Mattei, D. Schuhmacher, V. A. Yakovlev, A. A. Fedyanin, and O. A. Aktsipetrov, "Giant second harmonic generation in microcavities based on porous silicon photonic crystals," *JETP Lett.* **73**, 6–9 (2001) [*Pis'ma Zh. Eksp. Teor. Fiz.* **73**, 8–12 (2001)].
19. M. Born and E. Wolf, *Principles of Optics* (Pergamon, New York, 1964), p. 77.
20. J. P. Dowling, M. Scalora, M. J. Bloemer, and C. M. Bowden, "The photonic band edge laser: a new approach to gain enhancement," *J. Appl. Phys.* **75**, 1896–1899 (1994).
21. M. Scalora, M. J. Bloemer, A. S. Manka, J. P. Dowling, C. M. Bowden, R. Viswanathan, and J. W. Haus, "Pulsed second-harmonic generation in nonlinear, one-dimensional, periodic structures," *Phys. Rev. A* **56**, 3166–3174 (1997).
22. G. D'Aguanno, M. Centini, M. Scalora, C. Sibilias, Y. Dumeige, P. Vidakovic, J. A. Levenson, M. J. Bloemer, C. M. Bowden, J. W. Haus, and M. Bertolotti, "Photonic band edge

- effects in finite structures and applications to  $\chi^{(2)}$  interactions," *Phys. Rev. E* **64**, 016609–016609-9 (2001).
23. D. S. Bethune, "Optical harmonic generation and mixing in multilayer media: analysis using optical transfer matrix techniques," *J. Opt. Soc. Am. B* **6**, 910–916 (1989).
  24. M. J. Steel and C. Martijn de Sterke, "Second-harmonic generation in second-harmonic fiber Bragg gratings," *Appl. Opt.* **35**, 3211–3222 (1996).
  25. A. V. Balakin, V. A. Bushuev, B. I. Mantsyzov, I. A. Ozheredov, E. V. Petrov, A. P. Shkurinov, P. Masselin, and G. Mouret, "Enhancement of sum frequency generation near the photonic band gap edge under the quasiphase matching conditions," *Phys. Rev. E* **63**, 046609–0466011 (2001).
  26. J. Trull, R. Vilaseca, J. Martorell, and R. Corbalan, "Second-harmonic generation in local modes of a truncated periodic structure," *Opt. Lett.* **20**, 1746–1748 (1995).
  27. H. Cao, D. B. Hall, J. M. Torkelson, and C.-Q. Cao, "Large enhancement of second harmonic generation in polymer films by microcavities," *Appl. Phys. Lett.* **76**, 538–540 (2001).
  28. V. Pellegrini, R. Colombelli, I. Carusotto, F. Beltram, S. Rubini, R. Lantier, A. Franciosi, C. Vinegoni, and L. Pavesi, "Resonant second harmonic generation in ZnSe bulk microcavity," *Appl. Phys. Lett.* **74**, 1945–1947 (1999).
  29. T. V. Dolgova, M. G. Martemyanov, A. A. Fedyanin, O. A. Aktsipetrov, K. Nishimura, and M. Inoue, "Magnetization-induced second-harmonic generation and NOMOKE in magneto-photonic crystals and microcavities," in *Quantum Electronics and Laser Science*, Vol. 94 of OSA Trends in Optics and Photonics Series (Optical Society of America, Washington, D.C., 2002), p. 15.
  30. A. Yariv, Y. Xu, R. K. Lee, and A. Scherer, "Coupled-resonator optical waveguide: a proposal and analysis," *Opt. Lett.* **24**, 711–713 (1999).
  31. Y. Xu, R. K. Lee, and A. Yariv, "Propagation and second-harmonic generation of electromagnetic waves in a coupled-resonator optical waveguide," *J. Opt. Soc. Am. B* **17**, 387–400 (2000).
  32. S. Nakagawa, N. Yamada, N. Mikoshiba, and D. E. Mars, "Second-harmonic generation from GaAs/AlAs vertical cavity," *Appl. Phys. Lett.* **66**, 2159–2161 (1995).
  33. C. Simonneau, J. P. Debray, J. C. Harmand, P. Vidakovic, D. J. Lovering, and J. A. Levenson, "Second-harmonic generation in a doubly resonant semiconductor microcavity," *Opt. Lett.* **22**, 1775–1777 (1997).
  34. C. Mazzoleni and L. Pavesi, "Application to optical components of dielectric porous silicon multilayers," *Appl. Phys. Lett.* **67**, 2983–2985 (1995).
  35. O. Bisi, S. Ossicini, and L. Pavesi, "Porous silicon: a quantum sponge structure for silicon based optoelectronics," *Surf. Sci. Rep.* **38**, 1–126 (2000).
  36. V. Pellegrini, A. Tredicucci, C. Mazzoleni, and L. Pavesi, "Enhanced optical properties in porous silicon microcavities," *Phys. Rev. B* **52**, R14328–R14331 (1995).
  37. L. Pavesi, G. Panzarini, and L. C. Andreani, "All-porous silicon-coupled microcavities: experiment versus theory," *Phys. Rev. B* **58**, 15794–15800 (1998).
  38. L. A. Kuzik, V. A. Yakovlev, and G. Mattei, "Raman scattering enhancement in porous silicon microcavity," *Appl. Phys. Lett.* **75**, 1830–1832 (1999).
  39. T. V. Dolgova, A. I. Maidikovskiy, M. G. Martemyanov, A. A. Fedyanin, and O. A. Aktsipetrov, "Giant third-harmonic generation in photonic crystals and microcavities based on porous silicon," *JETP Lett.* **75**, 15–19 (2002) [*Pis'ma Zh. Eksp. Teor. Fiz.* **75**, 17–27 (2002)].
  40. W. Theiss, "Optical properties of porous silicon," *Surf. Sci. Rep.* **29**, 91–192 (1997).
  41. O. A. Aktsipetrov, A. V. Melnikov, Yu. N. Moiseev, T. V. Murzina, C. W. van Hasselt, Th. Rasing, and G. Rikken, "Second harmonic generation and atomic-force microscopy studies of porous silicon," *Appl. Phys. Lett.* **67**, 1191–1193 (1995).
  42. M. Falasconi, L. C. Andreani, A. M. Malvezzi, M. Patrini, V. Mulloni, and L. Pavesi, "Bulk and surface contributions to second-order susceptibility in crystalline and porous silicon by second-harmonic generation," *Surf. Sci.* **481**, 105–112 (2001).
  43. M. Cardona, "Modulation spectroscopy," in *Solid State Physics*, F. Seitz, D. Turnbull, and H. Ehrenreich, eds. (Academic, New York, 1969), Suppl. 11, Chap. 2.
  44. N. Bloembergen and P. S. Pershan, "Light waves at the boundary of nonlinear media," *Phys. Rev.* **128**, 606–622 (1962).
  45. N. Bloembergen, R. K. Chang, S. S. Jha, and C. H. Lee, "Optical second-harmonic generation in reflection from media with inversion symmetry," *Phys. Rev.* **174**, 813–822 (1968).